

Article

The Lower Atmospheric Characteristics of Dust Storms Using Ground-Based Sensor Data: A Comparative Analysis of Two Cases in Jinan, China

Tian Li ^{1,*} , Chenghao Tan ^{2,3}, Zilong Zhao ¹ and Wenjiao Yao ¹

¹ Jinan Meteorological Bureau, Jinan 250102, China; zhaozilong@jn.shandong.cn (Z.Z.); yaowenjiao18@mails.ucas.ac.cn (W.Y.)

² State Key Laboratory of Organic Geochemistry, Guangzhou Institute of Geochemistry, Chinese Academy of Sciences, Guangzhou 510640, China; tanchenghao@gig.ac.cn

³ University of Chinese Academy of Sciences, Beijing 100049, China

* Correspondence: litian@jn.shandong.cn

Abstract: Two severe dust storm (DS) events (15–17 March and 28–29 March) hit northern China in 2021 consecutively. The lower atmospheric vertical dynamic and thermal structures during the two cases were compared using the ground-based sensor data from the microwave radiometer and radar wind profiler, combined with the environmental and meteorological observations data in Jinan, China. It was found that both cases occurred under the background of cold vortexes over northeastern China. The dust was transported through the cold air on the northwest route. During the dust period, 2–3 km was the west or northwest airflow, and below 2 km was the northeast wind. The variation in the dynamic structure determined the duration of the DS. During the DS maintenance phase, the vertical wind shear (VWS) below 3 km measured approximately $10 \text{ m} \cdot (\text{s} \cdot \text{km})^{-1}$. The increased VWS during the dust intrusion period facilitated the transportation of dust. In contrast, the more significant VWS was not conducive to the maintenance of DS, and the shift to south wind control in the upper middle layer indicated the weakening of DS. In both cases, we observed a cliff-like decrease in relative humidity as a prominent indicator of dust outbreaks, occurring approximately 2–5 h beforehand. The diurnal difference between the vertical temperature and relative humidity during the dust maintenance period was found to be insignificant.

Keywords: dust storm; lower atmosphere; ground-based sensor; dynamics; thermal; China



Citation: Li, T.; Tan, C.; Zhao, Z.; Yao, W. The Lower Atmospheric Characteristics of Dust Storms Using Ground-Based Sensor Data: A Comparative Analysis of Two Cases in Jinan, China. *Atmosphere* **2024**, *15*, 282. <https://doi.org/10.3390/atmos15030282>

Academic Editors: Haoran Liu, Wei Tan and Wenjing Su

Received: 31 January 2024

Revised: 22 February 2024

Accepted: 23 February 2024

Published: 26 February 2024



Copyright: © 2024 by the authors. Licensee MDPI, Basel, Switzerland. This article is an open access article distributed under the terms and conditions of the Creative Commons Attribution (CC BY) license (<https://creativecommons.org/licenses/by/4.0/>).

1. Introduction

Air pollution events such as dust storms have recently received increasing international attention. Their increasing frequency and severity pose significant challenges to human health, agricultural productivity, and the ecological environment [1]. Detailed studies of the lower atmospheric conditions using various observation methods have been performed to understand the formation and transmission mechanism of dust storms [2–4]. The impacts of dust storm (DS) events on the physical and chemical processes show that the particles in the DS could affect the chemical reaction and energy balance in the boundary layer, further causing harm to the environment and ecosystem [5,6]. Researchers also identified key factors that contribute to the occurrence and severity of DS, such as climate change, land use change, and anthropogenic activities [7,8]. Remote sensing data are widely used in the study of the origin and transport trajectories of the dust, such as MODIS (Modify Resolution Imaging Spectrometer), CALIPSO (Cloud-Aerosol Lidar Infrared Pathfinder Satellite Observation), and the Fengyun Satellite series, providing researchers with more data options [9–12]. In addition to satellite remote sensing data, ground-based remote sensing data are also broadly used to detect different weather. They have high temporal and vertical resolution and can conduct continuous profiles of the atmospheric layer under

different weather conditions [13]. In recent years, as the China Meteorological Administration has successively started networking on new observation equipment, it is feasible and effective to explore the vertical structure of the atmosphere by using new data such as microwave radiometers and radar wind profilers [14–17].

In China, dust storms mainly occur in arid and semiarid areas such as the South Xinjiang Region, the Hexi Region, and their neighboring areas [18]. Based on data from 1980 to 2005, Zhang and Gao [19] found there were mainly three potential dust sources affecting northern China, and approximately 70% of the DS events impacting China originated from Mongolia. Bao et al. [20] investigated the spatiotemporal variations of border-crossing dust events between Mongolia and Inner Mongolia and supported the results that the sand and dust from Mongolia play a major contribution to the DS events in China. Previous investigations have been conducted on the vertical structure during the dust period in arid and semiarid areas of China. The vertical structure plays a crucial role in facilitating the mixing of dust aerosols [21]. By using the ground-based polarization Raman lidar, Zhang et al. [22] demonstrated that dust aerosols in the central Taklimakan Desert were regularly lifted over 6 km during the summer, while the majority of the dust remained restricted within 2 km. Based on the CALIPSO data analysis conducted in March 2021, Ye et al. [23] revealed that the dust conveyance height was mostly concentrated at 1–3 km and 3–10 km. By using microwave radiometer data from 2007 to 2013, Li et al. [24] discovered that before the occurrence of DS weather, there was a significant increase in temperature at the lower levels and a notable temperature decrease at higher altitudes in China's semi-arid region. By utilizing atmospheric aerosol lidar, Yin [25] indicated that during the period of sand and dust pollution in May 2022 in Xinjiang Province, the trend of $PM_{2.5}$ and PM_{10} was consistent, and there was heterogeneity in vertical height.

In March 2021, a series of severe dust storms occurred in northern China. Many scholars have studied these DS cases in terms of the causes, transport, deposition, and radiation effects. Liang et al. [9] found that the “3.15” DS radiated from central and southern Mongolia to northern China. The significant contribution of Mongolian sand also received validation in the March 2021 case. Zhang et al. [26] studied the vertical diffusion mechanism of the boundary layer in Beijing during the transport of DS and pointed out that the eruption of turbulence under the influence of a cold front led to a sharp increase in the dust concentration on the surface, while the continuous turbulence caused the dust to dissipate gradually. By comparing the three dust events in March 2021, Wang et al. [27] revealed the effect of the vertical structure of the atmosphere on the dust concentration and found that the continuous strong downdraft led to the sharp rise of the dust concentration near the ground. Gui et al. [28] compared the optical characteristics of the dust processes of “3.15” and “3.27” and found that the direct forcing of short-wave radiation caused by the dust particles in the latter was stronger than that of the former. Jin et al. [29] simulated the dust events and found that 69% of the dust deposition in the North China Plain came from long-distance transport from Mongolia. Song et al. [30] investigated the carbonaceous components, inorganic elements, and water-soluble ions in dust storms, providing diverse evidence for dust source identification.

Based on the above investigations, research predominantly relies on conventional observational data for analysis. Existing studies primarily focus on individual DS case analyses employing a single observational instrument. There is relatively little research on the lower atmospheric characteristics of downstream areas in the dust case. The lower atmospheric vertical structure of DS remains unclear. Therefore, it is imperative to investigate the structural characteristics of the local vertical atmosphere in dust transport utilizing novel high-resolution data. Jinan (JN), the capital of Shandong Province, is at the lower reaches of the Beijing–Tianjin–Hebei region. It is one of the main downstream affected areas in the transmission process of dust storms. Affected by the dust transport in the upstream area, there were two large-scale dust events in Jinan on March 15–18 and March 28–29, 2021, which are only about 10 days apart. Although the circulation backgrounds affecting

the two processes were similar, the intensity and duration of the two dust storms affecting Jinan were different. What were the influencing factors in the lower atmosphere?

This study explored the reasons mainly using high-resolution ground-based sensor data. In Section 2 of this paper, we introduce the high-resolution ground-based sensor data and methods. In Section 3, results are analyzed and discussed, including the comparisons of the ground meteorological elements, the intensity of cold air, and the vertical dynamic and thermodynamic structures. Lastly, the conclusions are summarized. Our ultimate purpose is to quantitatively understand the lower atmospheric vertical characteristics in the process of downstream dust invasion, maintenance, and dissipation.

2. Data and Methods

2.1. Ground-Based Remote Sensing Data

The two sources of ground-based remote sensing data are from the Chinese-made QFW-6000 microwave radiometer (MWR) and the CLC-11-F tropospheric radar wind profiler (RWP) installed in Pingyin, Jinan. The temporal resolution of temperature and relative humidity (RH) profiles of the MWR (116.41° E, 36.26° N) is 5 min, with a height resolution of 100 m (<2 km) and 250 m (2–10 km). The RWP (116.24° E, 36.15° N) provides the horizontal wind direction, horizontal wind speed, and vertical wind speed products with a time interval of 6 min. All the MWR and RWP data were under strict quality control for data consistency, continuity, and deviation based on the national standard of observation.

2.2. Environmental and Meteorological Data

The hourly meteorological observations were derived from the Chinese-made DZZ4 automatic weather device at JN National Meteorological Station. They include the surface temperature, pressure, relative humidity, wind direction, and wind speed. We also collected the 0.25° × 0.25° ERA5 reanalysis data from the ECMWF (European Center for Medium-Range Weather Forecasting) website to analyze the weather situation of the DS. The JN observational data of hourly PM₁₀ were observed by the Met One BAM-1020 particulate substance monitor from the National Air Quality Monitoring Network.

2.3. Methods

The vertical wind shear (VWS) and the vertical temperature lapse rate (VTLR) are important indicators of the lower atmosphere's dynamics and thermodynamics, respectively [13,31]. We used the VWS to characterize the wind shear intensity between two heights. Hourly VWS was calculated with the resolution of 120 or 240 m, expressed as follows:

$$VWS = \frac{\sqrt{(u_{z1} - u_{z2})^2 + (v_{z1} - v_{z2})^2}}{(z_1 - z_2)} \times 1000 \quad (1)$$

where VWS is the vertical wind shear (m·(s·km)⁻¹). u_{z1} and u_{z2} represent the zonal wind at z_1 and z_2 , and v_{z1} and v_{z2} denote the meridional wind at z_1 and z_2 , respectively ($z_2 > z_1$).

The VTLR (°C·hm⁻¹) is defined as:

$$\gamma = -\frac{T_{z2} - T_{z1}}{z_2 - z_1} \times 100 \quad (2)$$

where γ is the vertical temperature lapse rate. T_{z1} and T_{z2} represent the temperature at z_1 and z_2 , respectively ($z_2 > z_1$).

3. Results and Discussion

3.1. Surface Elements Changes

For the convenience of expression, we referred to the former dust process as “case 1” and the latter as “case 2”. According to the hourly variations of PM₁₀ concentrations, we divided the dust storm episode into three periods, corresponding to invasion (Period 1,

P1), maintenance (Period 2, P2), and dissipation (Period 3, P3). In case 1 (Figure 1a), the minimum visibility was 1.0 km, and the PM₁₀ peak reached 1146.8 µg/m³. The intensity of case 2 (Figure 1b) was slightly weaker, but the peak value of PM₁₀ still reached 1101.2 µg/m³ with a minimum visibility of 1.9 km. Both cases show that RH appeared to have a cliff-like decrease during the P1. In case 1, as PM₁₀ started to rocket at 17:00 on the 15th, the RH decreased from 80% to 35% within 4 h. Meanwhile, in case 2, the RH decreased from 73% to 46% within 3 h from 11:00 on the 28th. Before the P1, the southerly wind dominated. A significant shift in the surface wind direction occurred during P1. As the cold air blew southward, the northeasterly wind dominated. The northeasterly wind gradually weakened, turning south during P3. The surface wind speed in P2 was slightly lower than that in P1. The cold air intrusion periods in the two cases were both afternoons, but the surface temperature before P1 in case 2 was 18.2 °C, which was 4 °C higher than in case 1.

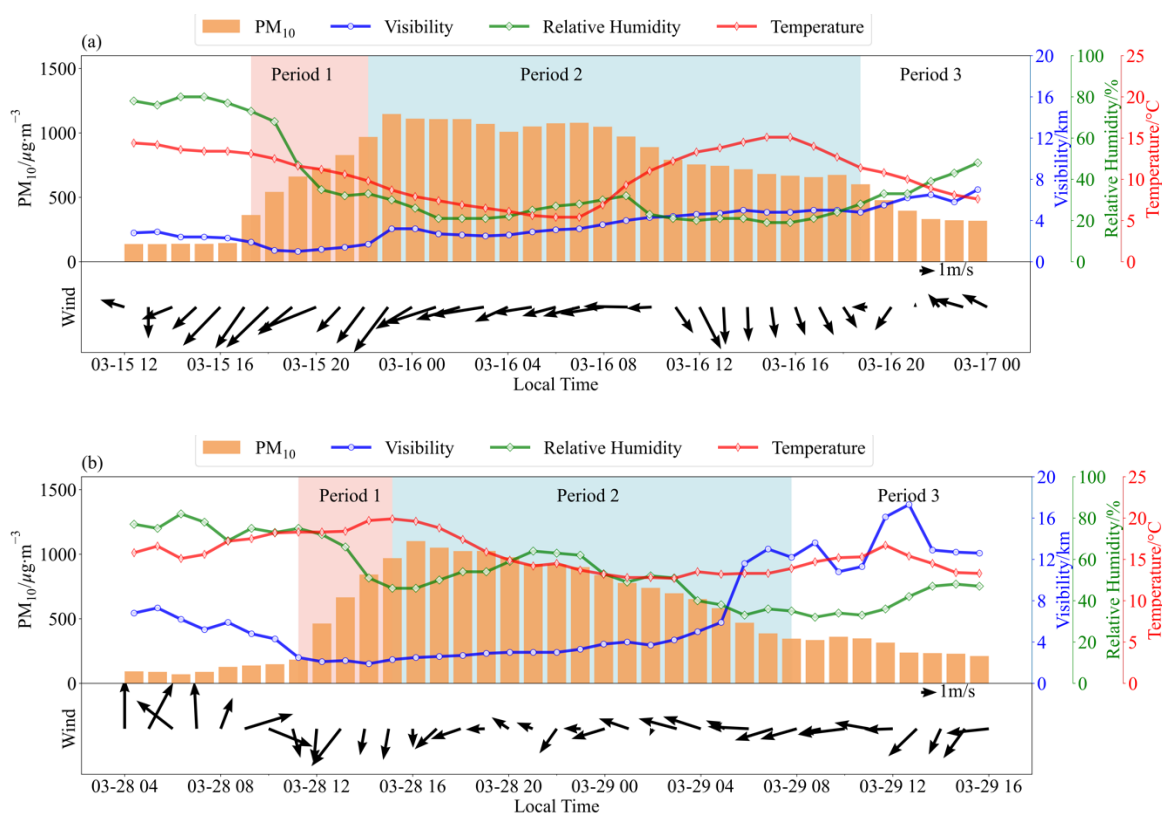


Figure 1. Hourly variations of PM₁₀ concentrations and surface meteorological elements during the two cases. (a) From 12:00 on 15 March to 00:00 on 17 March 2021; (b) from 04:00 on 28 March to 16:00 on 29 March 2021.

3.2. Cold Air Intensity

The DS events we discussed were both affected by the transport and deposition of high-altitude dust. Both cases were formed under similar circulation patterns, as Figure 2 demonstrates. At 500 hPa, the cold vortex was located over the northeast (between 115° E–120° E, 45° N–50° N). The northwest airflow controlled JN at the base of the cold vortex. Case 1's 500 hPa closed isotherm center was measured at −32 °C, but case 2's cold center was slightly weaker at −28 °C. In each case, the temperature field trailed behind the height field, causing a blast of cold air to break through the North China Plain and head south. In comparison to case 2, case 1's cold air influence range and intensity were noticeably larger. At 08:00 on March 15, there was a strong temperature front and an intense cold advection center (-10×10^{-4} °C/s) near 42° N, with northwest wind speeds ranging from 12–18 m/s. The isobars and isotherms at 500 hPa in the upstream region (Jing–Jin–Ji) were dense (Figure 2a).

The northwest wind speed ranged from 8 to 12 m/s, and the corresponding surface cold advection center intensity was $-7 \times 10^{-4} \text{ }^\circ\text{C/s}$ (Figure 2c). At 8:00 on March 28, the highest cold advection on the ground was only $-4 \times 10^{-4} \text{ }^\circ\text{C/s}$ (Figure 2d), while the center of the cold advection at 850 hPa was $-10 \times 10^{-4} \text{ }^\circ\text{C/s}$ (Figure 2b). Compared to case 1, the surface wind speed in case 2 was approximately 2–4 m/s slower. In summary, the cold air intensity of case 1 was stronger than that in case 2. Later, a more thorough comparison and analysis of the lower atmospheric structure during the dust transmission is conducted.

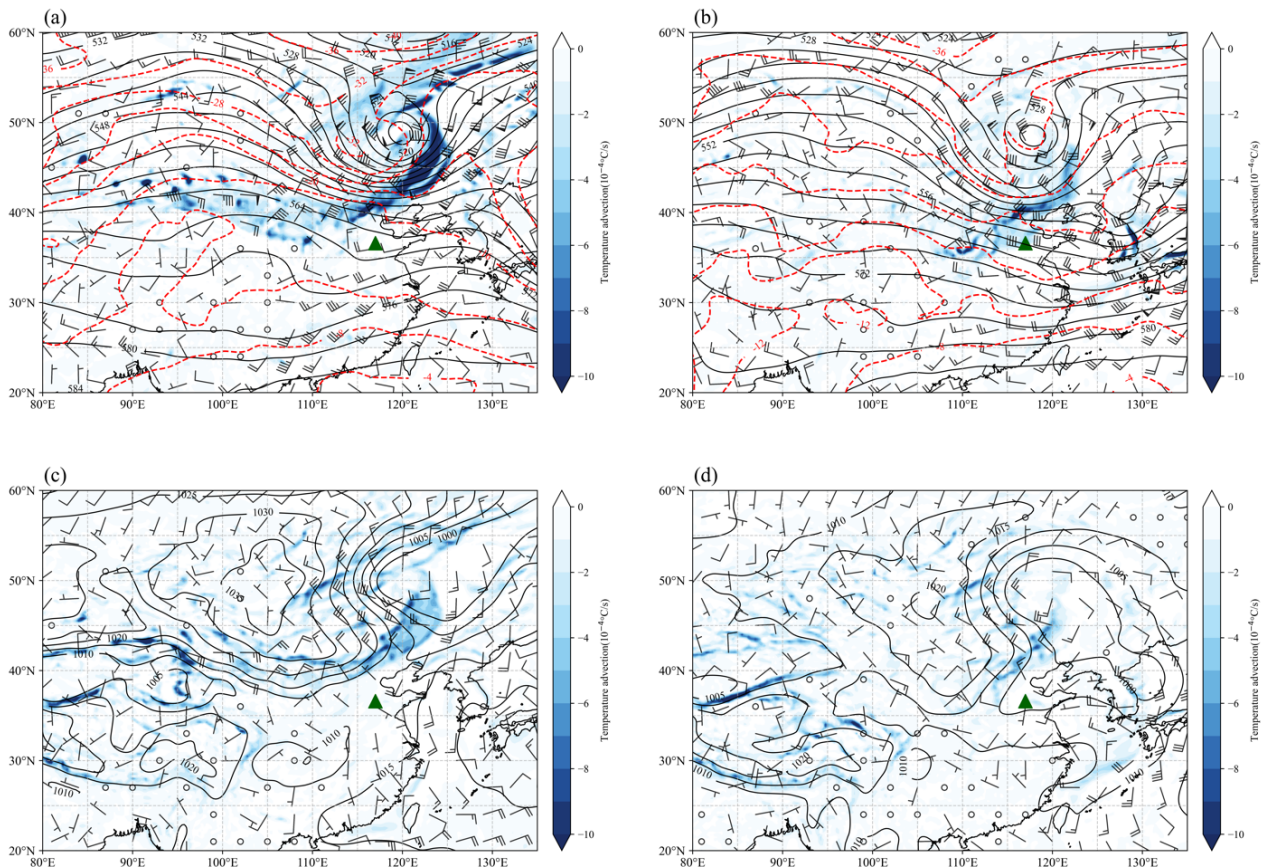


Figure 2. The 500 hPa geopotential height fields, 500 hPa temperature fields (red line), 850 hPa wind vectors, and 850 hPa temperature advection (shaded) at 08:00 on 15 March (a) and 08:00 on 28 March 2021 (b). The sea-level pressure fields, 10 m wind fields, and 2 m temperature advection (shaded) at 08:00 on 15 March (c) and 08:00 on 28 March 2021 (d). The green triangle represents Jinan.

3.3. Dynamic and Thermodynamic Structure in the Lower Atmosphere

In this section, we characterize the lower atmospheric characteristics of the three periods in the two cases using the RWP and MWR data. Under a similar cold vortex background, the wind field structure below 3 km in both cases presented the characteristics of “backflow”. In case 1, the northwest airflow was between 2 and 3 km, while the northeast wind was less than 1.5 km. The wind direction is reversed counterclockwise with heights (Figure 3a). In case 2, the characteristics of “backflow” are more typical, with west-northwest airflow at 2–3 km and northeast wind below 2 km. In case 1, a weak descending motion ($0.8 \text{ m}\cdot\text{s}^{-1}$) occurred both before and during the P2, which was conducive to dust deposition. There was a clear northeast jet within 0–700 m from 16:00 on the 15th to the early hours of the following day, which was also helpful for the ongoing transport of dust.

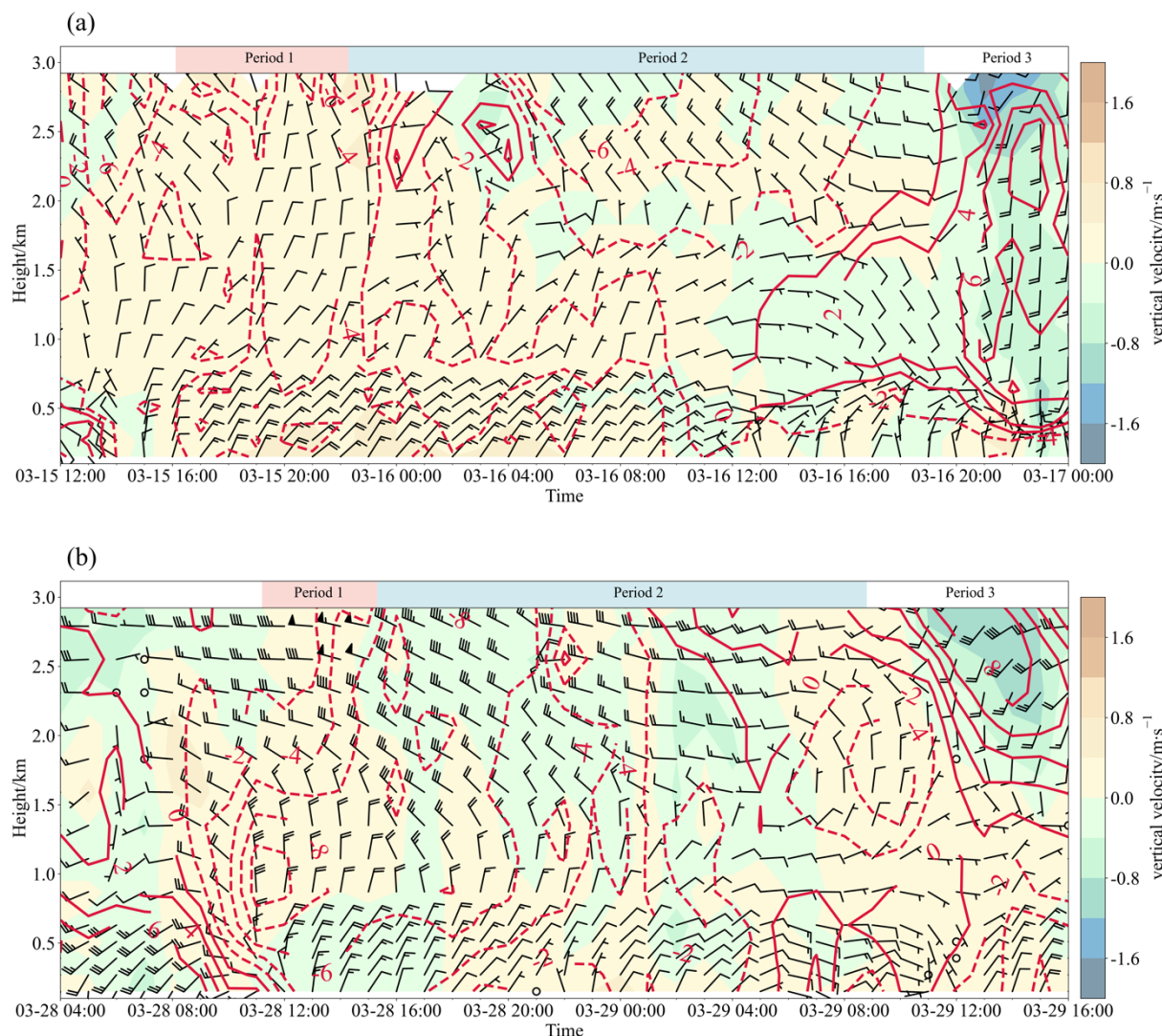


Figure 3. Hourly variations of 0–3 km wind profile, northerly wind component (red line), and vertical velocity (shaded, positive value indicates descending motion) from (a) 12:00 on 15 March to 00:00 on 17 March 2021 and (b) 4:00 on 28 March to 16:00 on 29 March 2021.

In case 2 (Figure 3b), there was a significant downward momentum transportation during the P1. At approximately 12:00 on March 28, a maximum wind speed center of $16\text{--}20\text{ m}\cdot\text{s}^{-1}$ was observed at an altitude of 2.5–3 km. The center rapidly decreased over time, accompanied by a gradual grounding and rotation of wind direction. This was conducive to dust transport and deposition of the dust. Four hours later (at 16:00 on March 28), the PM₁₀ concentration on the ground reached the maximum (Figure 1b). However, in case 1, the downward momentum transportation was weak during the dust invasion period (Figure 3a). In case 2, the ascending and descending movements alternated in the dust-influenced stage, which was conducive to dust maintenance. In addition, the north wind component (red line) also played an important role in dust transportation. The north wind component of the two cases was maintained between 4 and $8\text{ m}\cdot\text{s}^{-1}$ in the dust invasion and maintenance (P1 and P2). Before and after the two cases dissipated, the wind above 2 km first turned to the south (the north wind component was positive), signifying that the influence of cold air transmission had ended. This indicated that the influence of the dust storm tended to weaken or terminate.

VWS signifies the state of vertical dynamic mixing in the atmosphere, which plays a vital role in both pollutant accumulation and diffusion. To analyze the vertical characteristics of the dynamic structure in the lower atmosphere during various periods of the DS, we

calculated the mean profiles of VWS and north wind components, as depicted in Figure 4. The VWS and northerly wind components of the two cases exhibited distinct characteristics with heights. Both P1 and P2 were affected by northerly wind transport (Figure 4d,e). Although the cold air intensity of case 1 was stronger (Section 3.2), the northerly wind component was weaker than that of case 2. In P3, the upper-middle level (1–3 km) wind first turned to the south (Figure 4f). There was little difference between the VWS in P1 and P2 of case 1. However, the VWS of P1 in case 2 was significantly larger than that in P2, especially when the VWS increased to about $15 \text{ m}\cdot(\text{s}\cdot\text{km})^{-1}$ at the height of 1.5–2.5 km, resulting in explosive growth of dust concentrations. The VWS in P2 of both processes was about $10 \text{ m}\cdot(\text{s}\cdot\text{km})^{-1}$. In the P3, the VWS over 2 km increased to $10\text{--}20 \text{ m}\cdot(\text{s}\cdot\text{km})^{-1}$ in both cases (Figure 4c). Additionally, there was an observed increase in the southerly wind component over 2 km (Figure 4f, the northerly wind component turned positive). This indicated that the wind direction shifting to the south and large VWS over 2 km was conducive to the dust dissipation.

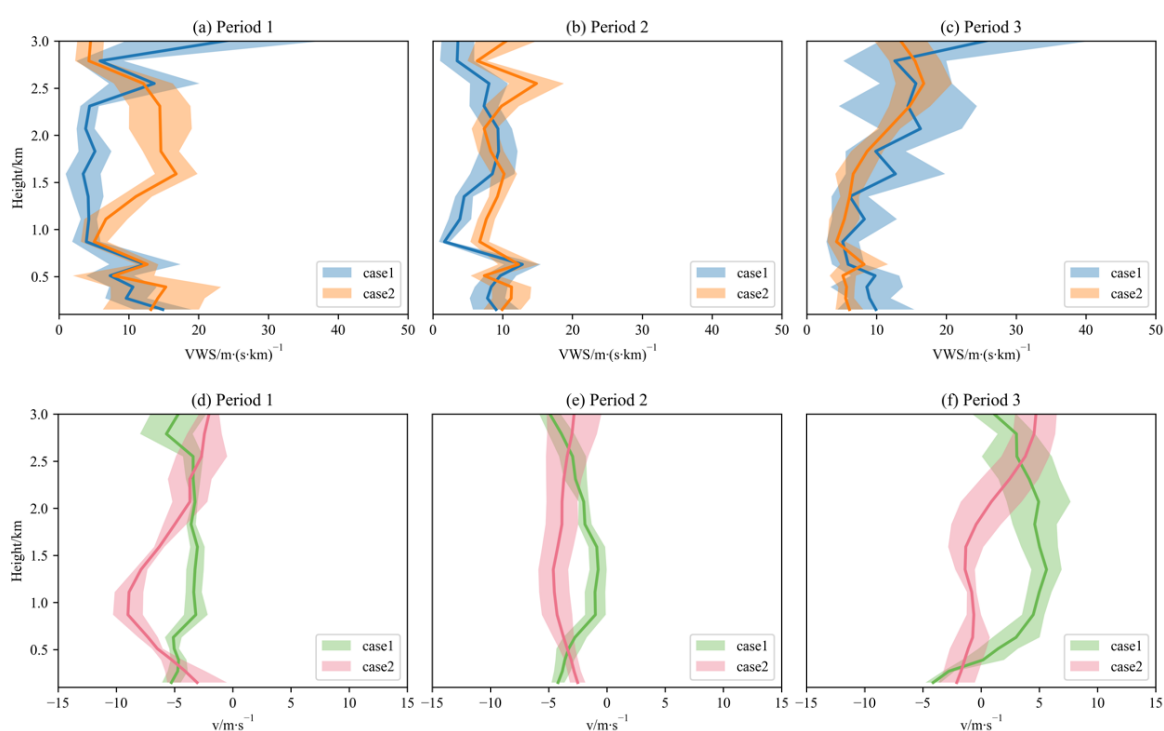


Figure 4. (a–c) Mean profiles of 0–3 km vertical wind shear (VWS) ($\text{m}\cdot(\text{s}\cdot\text{km})^{-1}$), and (d–f) northerly wind components ($\text{m}\cdot\text{s}^{-1}$) during the dust invasion, maintenance, and dissipation periods of the two cases (shadows represent 95% confidence intervals for the mean).

By comparing the vertical structural changes of RH and temperature retrieved by MWR in the two cases (Figure 5), a common feature can be found: the RH in the lower atmosphere before the dust intrusion showed a cliff-like decline. As can be seen from Figure 1, the PM_{10} concentration peaked at 23:00 on March 15 and 16:00 on March 28, respectively, while the RH profiles showed an obvious decline at 18:00 on March 15 (Figure 5a) and around 14:00 on March 28 (Figure 5b). Meanwhile, the maximum value area of the humidity gradient first appeared near 1.5–2.5 km, which was at least 2–5 h earlier than the peak dust concentration on the ground. Thus, a cliff-like decrease in RH about 2 km, occurring 2–5 h beforehand, serves as an indicator of an abrupt increase in dust concentrations. During these two cases, the height of dust transport in the upstream Beijing area varied from 1 to 2.5 km [32]. Affected by the northwest cold air transmission, the downstream area of Jinan will inevitably experience dust transportation followed by deposition. The height of approximately 2 km may be where the sand and dust first invaded, so this altitude range will first appear as a cliff-like drop in RH. During case 1, the isotherms (red line) exhibited

a continuous decrease, whereas in case 2, they displayed a minor peak. The explanation for this phenomenon is as follows. In case 1, the solar radiation warming near the ground was weakened with time, and the temperature in the lower atmosphere gradually decreased due to the influence of cold air transmission. However, during case 2, a weak cold air mass combined with surface heat absorption at noon to produce a small temperature peak at approximately 15:00.

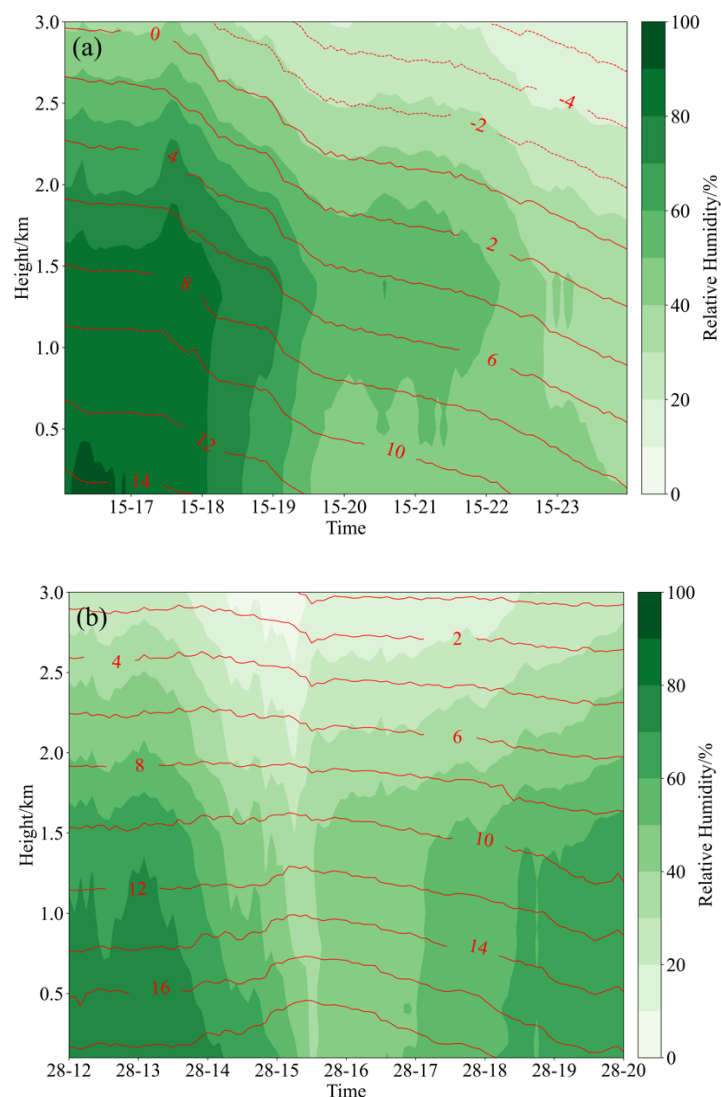


Figure 5. Temporal profile distributions of 0–3 km relative humidity (shadow, %) and temperature (red line, °C) near the dust intrusion in two cases. (a) From 16:00 to 24:00 on 15 March 2021; (b) From 12:00 to 20:00 on 28 March 2021.

The maintenance period (P2) of the two dust cases both went through day and night. Therefore, the thermal structure at 0–3 km is represented by the mean profiles of the RH and VTLR in day and night, respectively, as shown in Figure 6. The times 08:00 and 20:00 are taken as the dividing time points of day and night. In Figure 6a,b, the RH of the two cases had a large difference below 1.5 km and a small difference above 1.5 km. The difference between the mean RH values at each height during the day was at most 20%, while the difference at night was at most 15%. In the same case, the RH of day and night showed a similar shape with heights. The maximum was concentrated below 1.5 km, and the difference between day and night at each height was not large (the maximum is about 15%). However, by comparing with the 25–75% percentile value, we found that the fluctuation range of the RH during the day was larger than that at night. During the dust maintenance

period, the RH in the lower layer decreased and remained at a low value, so the diurnal difference in the humidity profile was small. During the day, as the solar radiation first increased and then weakened, the RH also fluctuated, resulting in a wider range of changes in the daytime. As shown in Figure 6c,d, there was little difference between day and night in the VTLR in the dust maintenance period. It was maintained at approximately $0.5\text{ }^{\circ}\text{C}\cdot\text{hm}^{-1}$ and oscillated more dramatically below 2 km. In summary, during the dust maintenance periods, the vertical temperature and relative humidity changes during the day and night were significantly small.

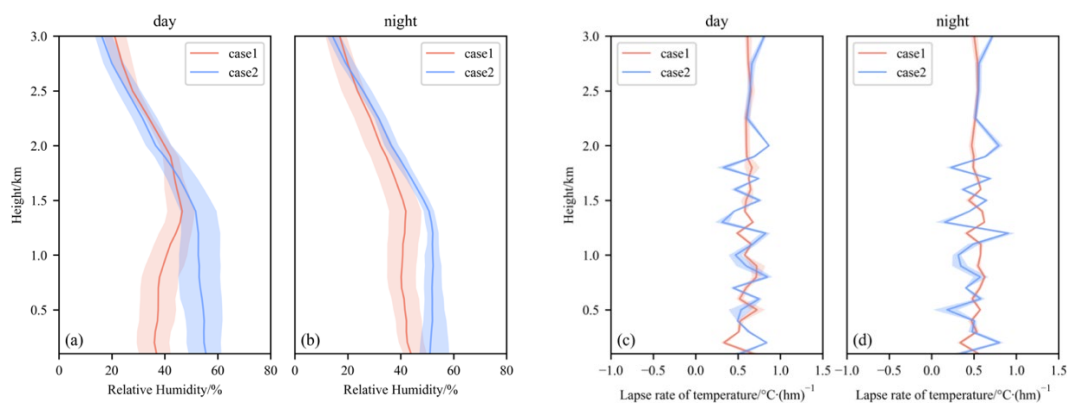


Figure 6. (a,b) Mean profiles of relative humidity and (c,d) temperature lapse rate during the day and night in the dust maintenance period (shadows represent the 25–75% percentiles).

4. Discussion and Conclusions

According to statistics provided by the China Meteorological Administration, a total of 37 large-scale and intense dust storm (DS) events occurred in northern China between 2000 and 2023, averaging approximately 1.5 occurrences per year. These events were predominantly observed from March to May. The most severe dust storm event in Jinan was notably observed in March 2021, subsequent to the year 2010. Our research utilized the MWR and RWP data to compare the vertical dynamic and thermal structure of the lower atmospheric layer in two dust events that occurred in March 2021 in Jinan, China. The two cases we studied during this period (March 15–18 and March 28–29) are representative. Gao et al. [33] have suggested that the dust storm frequency is tightly linked to the atmospheric general circulations, and the cyclones are believed to play a dominant role in causing the DS events in northern China. We found a similar pattern causing these two DS events in this study. Both cases occurred under the influence of the northeastern cold vortex.

Then, we examined the impacts of the dynamic structure within the lower atmosphere during the DS events. The change of wind direction is a critical point for the different periods of the DS. As the most important dynamic condition, strong northerly wind has a significant positive correlation with the spring dust storm frequency [34]. The dust weather was generated through the transmission of cold air under the influence of the northwest airflow. The west–northwest airflow is 2–3 km, and the northeasterly wind is below 2 km. In both cases, the initial shift to the south wind control above 2 km was observed at the beginning of the dissipation period, indicating the dust would weaken. The VWS increases rapidly in both the invasion and dissipation periods of the dust. The VWS in the dust maintenance stage of both cases was about $10\text{ m}\cdot(\text{s}\cdot\text{km})^{-1}$. The typical feature of case 1 was that there was a boundary layer jet with a wind speed of approximately $8\text{ m}\cdot\text{s}^{-1}$ at 0–700 m. This phenomenon was conducive to dust transport. Case 2 was characterized by a noticeable downward momentum at 2.5–3 km, which was favorable for the sharp increase in dust concentration. In addition, this finding was in line with the study conducted by Wang et al. [27], which examined a typical dust storm event in Beijing and proposed that the intensity of vertical downdraft directly influenced the amount of dust deposition on the ground.

The MWR is an effective method to detect the vertical thermodynamic characteristics at different heights in DS events. Our analysis suggested the change features of relative humidity before the dust concentration sharply rises, consistent with Hao et al. [35]. They found that the overall atmospheric humidity showed a steep decline trend before the particulate concentration on the ground increased dramatically in Xingtai, Hebei Province. However, we conducted further investigation into the indicative characteristics of height and time, and the results may have broader implications and significance. The maximum value of the humidity gradient first appeared near 1.5–2.5 km. If the relative humidity in this height range shows a cliff-like decline, it signifies that the dust concentration will rise sharply within 2–5 h. In addition, during the dust maintenance period, the diurnal difference in the vertical structure of temperature and humidity in the lower atmospheric layer was found to be small. However, the fluctuation range of relative humidity in the daytime was larger than that at night.

Overall, based on the two ground-sensor data sources, this study reveals the structural characteristics of the lower atmosphere in the downstream region during the dust transport process. It is important to note that our conclusions are specific to these two cases and should not be generalized. Therefore, we plan to carry out further investigations to explore more dust events by employing a wider range of ground sensor instruments or numerical simulations, thereby enhancing our understanding of the dust transport mechanism.

Author Contributions: T.L.: conceptualization, methodology, investigation, writing of original draft, funding acquisition, writing–review and editing, software. C.T.: conceptualization, investigation, methodology, resources. Z.Z.: conceptualization, methodology, data curation, W.Y.: resources, software. All authors have read and agreed to the published version of the manuscript.

Funding: Supported by the National Natural Science Foundation of China (42075186, 41830965, 42275196), the projects of Shandong Meteorological Bureau (2020SDQN12, 2021SDYD23, 2023sdqxz14), and the projects of Jinan Meteorological Bureau (2024jnxzdz01).

Institutional Review Board Statement: Not applicable.

Informed Consent Statement: Not applicable.

Data Availability Statement: The data underlying the results presented in this paper are available by contacting the corresponding author. The ERA5 reanalysis data are from <https://cds.climate.copernicus.eu/>, accessed on 11 December 2022. The other data are not publicly available due to a confidentiality agreement with China Meteorological Administration.

Conflicts of Interest: The authors declare no conflict of interest.

References

1. Qian, W.; Tang, X.; Quan, L. Regional Characteristics of Dust Storms in China. *Atmos. Environ.* **2004**, *38*, 4895–4907. [CrossRef]
2. Niu, H.; Zhang, D.; Hu, W.; Shi, J.; Li, R.; Gao, H.; Pian, W.; Hu, M. Size and Elemental Composition of Dry-Deposited Particles during a Severe Dust Storm at a Coastal Site of Eastern China. *J. Environ. Sci.* **2016**, *40*, 161–168. [CrossRef] [PubMed]
3. Tiwari, S.; Kumar, A.; Pratap, V.; Singh, A.K. Assessment of Two Intense Dust Storm Characteristics over Indo-gangetic Basin and Their Radiative Impacts: A Case Study. *Atmos. Res.* **2019**, *228*, 23–40. [CrossRef]
4. Meng, L.; Yang, X.; Zhao, T.; He, Q.; Lu, H.; Mamtimin, A.; Huo, W.; Yang, F.; Liu, C. Modeling Study on Three-Dimensional Distribution of Dust Aerosols during a Dust Storm over the Tarim Basin, Northwest China. *Atmos. Res.* **2019**, *218*, 285–295. [CrossRef]
5. Uno, I.; Eguchi, K.; Yumimoto, K.; Takemura, T.; Shimizu, A.; Uematsu, M.; Liu, Z.; Wang, Z.; Hara, Y.; Sugimoto, N. Asian Dust Transported One Full Circuit around the Globe. *Nat. Geosci.* **2009**, *2*, 557–560. [CrossRef]
6. Tang, W.; Dai, T.; Cheng, Y.; Wang, S.; Liu, Y. A Study of a Severe Spring Dust Event in 2021 over East Asia with WRF-Chem and Multiple Platforms of Observations. *Remote Sens.* **2022**, *14*, 3795. [CrossRef]
7. Qian, W.; Quan, L.; Shi, S. Variations of the Dust Storm in China and Its Climatic Control. *J. Clim.* **2002**, *15*, 1216–1229. [CrossRef]
8. Lee, J.A.; Gill, T.E.; Mulligan, K.R.; Dominguez Acosta, M.; Perez, A.E. Land Use/Land Cover and Point Sources of the 15 December 2003 Dust Storm in Southwestern North America. *Geomorphology* **2009**, *105*, 18–27. [CrossRef]
9. Liang, P.; Chen, B.; Yang, X.; Liu, Q.; Li, A.; Mackenzie, L.; Zhang, D. Revealing the Dust Transport Processes of the 2021 Mega Dust Storm Event in Northern China. *Sci. Bull.* **2022**, *67*, 21–24. [CrossRef]
10. Yan, Y.; Sun, Y.; Ma, L.; Long, X. A Multidisciplinary Approach to Trace Asian Dust Storms from Source to Sink. *Atmos. Environ.* **2015**, *105*, 43–52. [CrossRef]

11. Huang, J.P.; Liu, J.J.; Chen, B.; Nasiri, S.L. Detection of Anthropogenic Dust Using CALIPSO Lidar Measurements. *Atmos. Chem. Phys.* **2015**, *15*, 11653–11665. [[CrossRef](#)]
12. Yang, L.; She, L.; Che, Y.; He, X.; Yang, C.; Feng, Z. Analysis of Dust Detection Algorithms Based on FY-4A Satellite Data. *Appl. Sci.* **2023**, *13*, 1365. [[CrossRef](#)]
13. Kotthaus, S.; Bravo-Aranda, J.A.; Collaud Coen, M.; Guerrero-Rascado, J.L.; Costa, M.J.; Cimini, D.; O'Connor, E.J.; Hervo, M.; Alados-Arboledas, L.; Jiménez-Portaz, M.; et al. Atmospheric boundary layer height from ground-based remote sensing: A review of capabilities and limitations. *Atmos. Meas. Tech.* **2023**, *16*, 433–479. [[CrossRef](#)]
14. Liu, B.; Guo, J.; Gong, W.; Shi, L.; Zhang, Y.; Ma, Y. Characteristics and performance of wind profiles as observed by the radar wind profiler network of China. *Atmos. Meas. Tech.* **2020**, *13*, 4589–4600. [[CrossRef](#)]
15. Miao, Y.; Che, H.; Zhang, X.; Liu, S. Relationship between Summertime Concurring PM_{2.5} and O₃ Pollution and Boundary Layer Height Differs between Beijing and Shanghai, China. *Environ. Pollut.* **2021**, *268*, 115775. [[CrossRef](#)]
16. Li, J.; Sun, Z.; Lenschow, D.H.; Zhou, M.; Dou, Y.; Cheng, Z.; Wang, Y.; Li, Q. A foehn-induced haze front in Beijing: Observations and implications. *Atmos. Chem. Phys.* **2020**, *20*, 15793–15809. [[CrossRef](#)]
17. Huang, J.; Liao, B.; Wang, C.; Tan, H.; Shen, Z.; Lan, J.; Tang, J.; Yue, H. Application of new vertical detection data in the analysis of a heavy pollution weather. *China Environ. Sci.* **2019**, *39*, 92–105. (In Chinese)
18. Wang, S.; Wang, J.; Zhou, Z.; Shang, K. Regional Characteristics of Three Kinds of Dust Storm Events in China. *Atmos. Environ.* **2005**, *39*, 509–520. [[CrossRef](#)]
19. Zhang, K.; Gao, H. The Characteristics of Asian-Dust Storms during 2000–2002: From the Source to the Sea. *Atmos. Environ.* **2007**, *41*, 9136–9145. [[CrossRef](#)]
20. Bao, T.; Gao, T.; Nandintsetseg, B.; Yong, M.; Jin, E. Variations in Frequency and Intensity of Dust Events Crossing the Mongolia–China Border. *SOLA* **2021**, *17*, 145–150. [[CrossRef](#)]
21. Sugimoto, N.; Hara, Y.; Shimizu, A.; Nishizawa, T.; Matsui, I.; Nishikawa, M. Analysis of Dust Events in 2008 and 2009 Using the Lidar Network, Surface Observations and the CFORS Model. *Asia-Pac. J. Atmos. Sci.* **2013**, *49*, 27–39. [[CrossRef](#)]
22. Zhang, S.; Huang, Z.; Li, M.; Shen, X.; Wang, Y.; Dong, Q.; Bi, J.; Zhang, J.; Li, W.; Li, Z.; et al. Vertical Structure of Dust Aerosols Observed by a Ground-Based Raman Lidar with Polarization Capabilities in the Center of the Taklimakan Desert. *Remote Sens.* **2022**, *14*, 2461. [[CrossRef](#)]
23. Ye, Q.; Zheng, X.; Zhao, S. Remote sensing monitoring and transport path analysis of an intense dust weather in northern China in 2021. *Natl. Remote Sens. Bull.* **2021**, *27*, 1821–1833. (In Chinese)
24. Li, N.; Zhang, W.; Che, Y.; Liu, D.; Shi, J.; Zhang, B. Remote-sensing of atmospheric temperature and relative humidity profiles based on microwave radiometer. *J. Lanzhou Univ. Nat. Sci.* **2015**, *51*, 61–71. (In Chinese)
25. Yin, L.; He, Q.; Li, J.; Meng, L.; Fu, X.; Wu, C.; Xiao, H.; Fan, X. Ground-based radar-based investigation of a sand and dust pollution process in Hotan City. *China Environ. Sci.* **2023**, *43*, 6290–6300. (In Chinese)
26. Zhang, L.; Zhang, H.; Li, Q.; Cai, X.; Song, Y. Vertical Dispersion Mechanism of Long-Range Transported Dust in Beijing: Effects of Atmospheric Turbulence. *Atmos. Res.* **2022**, *269*, 106033. [[CrossRef](#)]
27. Wang, F.; Yang, T.; Wang, Z.; Cao, J.; Liu, B.; Liu, J.; Chen, S.; Liu, S.; Jia, B. A Comparison of the Different Stages of Dust Events over Beijing in March 2021: The Effects of the Vertical Structure on Near-Surface Particle Concentration. *Remote Sens.* **2021**, *13*, 3580. [[CrossRef](#)]
28. Gui, K.; Yao, W.; Che, H.; An, L.; Zheng, Y.; Li, L.; Zhao, H.; Zhang, L.; Zhong, J.; Wang, Y.; et al. Record-breaking dust loading during two mega dust storm events over northern China in March 2021: Aerosol optical and radiative properties and meteorological drivers. *Atmos. Chem. Phys.* **2022**, *22*, 7905–7932. [[CrossRef](#)]
29. Jin, J.; Pang, M.; Segers, A.; Han, W.; Fang, L.; Li, B.; Feng, H.; Lin, H.X.; Liao, H. Inverse modeling of the 2021 spring super dust storms in East Asia. *Atmos. Chem. Phys.* **2022**, *22*, 6393–6410. [[CrossRef](#)]
30. Song, L.; Bi, X.; Zhang, Z.; Li, L.; Dai, Q.; Zhang, W.; Li, H.; Wang, X.; Liang, D.; Feng, Y. Impact of Sand and Dust Storms on the Atmospheric Environment and Its Source in Tianjin–China. *Sci. Total Environ.* **2022**, *825*, 153980. [[CrossRef](#)]
31. Sun, X.; Zhou, Y.; Zhao, T.; Bai, Y.; Huo, T.; Leng, L.; He, H.; Sun, J. Effect of Vertical Wind Shear on PM_{2.5} Changes over a Receptor Region in Central China. *Remote Sens.* **2022**, *14*, 3333. [[CrossRef](#)]
32. Zhai, L.; Lei, L.; Liu, R.; Li, L.; Sun, Z.; Li, Z. Comparison of removal mechanism in two typical dust processes. *Acta Sci. Circumstantiae* **2022**, *42*, 111–119. (In Chinese)
33. Gao, J.; Ding, T.; Gao, H. Dominant Circulation Pattern and Moving Path of the Mongolian Cyclone for the Severe Sand and Dust Storm in China. *Atmos. Res.* **2024**, *301*, 107272. [[CrossRef](#)]
34. Liu, X.; Yin, Z.-Y.; Zhang, X.; Yang, X. Analyses of the Spring Dust Storm Frequency of Northern China in Relation to Antecedent and Concurrent Wind, Precipitation, Vegetation, and Soil Moisture Conditions. *J. Geophys. Res. Atmos.* **2004**, *109*, D16. [[CrossRef](#)]
35. Hao, J.; Yuan, L.; Li, Z.; Qi, J.; Shi, H. The detection and analysis of dust weather by lidar and microwave radiometer in Xingtai. *Plateau Meteorol.* **2018**, *37*, 1110–1119. (In Chinese)

Disclaimer/Publisher’s Note: The statements, opinions and data contained in all publications are solely those of the individual author(s) and contributor(s) and not of MDPI and/or the editor(s). MDPI and/or the editor(s) disclaim responsibility for any injury to people or property resulting from any ideas, methods, instructions or products referred to in the content.